RESEARCH ARTICLE | AUGUST 09 2022

Predictive capability of the logarithmic law for roughness-modeled large-eddy simulation of turbulent channel flows with rough walls ⊘

Shilong Li (李世隆); Xiaolei Yang (杨晓雷) ✉ ; Yu Lv (吕钰)

Check for updates

CrossMark

View Online

Export Citation

Articles You May Be Interested In

The direct evaluation of a first-order rate constant from spectrophotometric data using (i) a logarithmic-logarithmic circuit, and (ii) a logarithmic-differentiator-logarithmic circuit
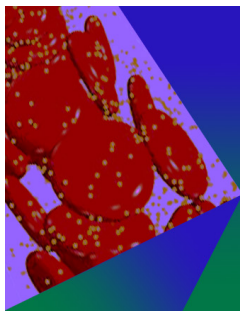
Rev Sci Instrum (November 2003)

Napier's logarithms

American Journal of Physics (February 2000)

Logarithmic Scales: A Useful Example

The Physics Teacher (January 2003)

Physics of Fluids

Special Topic: Flow and Forensics

Submit Today!

AIP Publishing

Predictive capability of the logarithmic law for roughness-modeled large-eddy simulation of turbulent channel flows with rough walls

View Online   Export Citation   CrossMark

Shilong Li (李世隆),[1,2] Xiaolei Yang (杨晓雷),[1,2,a] (iD) and Yu Lv (吕钰)[1,2]

AFFILIATIONS

[1]The State Key Laboratory of Nonlinear Mechanics, Institute of Mechanics, Chinese Academy of Sciences, Beijing 100190, China
[2]School of Engineering Sciences, University of Chinese Academy of Sciences, Beijing 100049, People's Republic of China

[a]Author to whom correspondence should be addressed: xyang@imech.ac.cn

ABSTRACT

Direct numerical simulation (DNS) and large-eddy simulation (LES) resolving roughness elements are computationally expensive. LES employing the logarithmic law as the wall model, without the need to resolve the flow at the roughness element scale, provides an efficient alternative for simulating turbulent flows over rough walls. In this work, we evaluate the predictive capability of the roughness-modeled LES by comparing its predictions with those from the roughness-resolved DNS for turbulent channel flows with rough walls. A good agreement is observed for the mean streamwise velocity. The Reynolds stresses predicted by the roughness-modeled LES also reasonably agree with the roughness-resolved predictions. Differences, on the other hand, are observed for the dispersive Reynolds stresses, integral scales, and space-time correlations. The roughness-modeled LES fails to predict the dispersive stresses as one can expect. In the outer layer, the integral length scale predicted by the roughness-modeled LES is lower than the roughness-resolved prediction, which cannot be improved by refining the grid. As for the space-time correlations, discrepancies are shown for the streamwise velocity fluctuations, with a faster decay of the correlation in the outer layer observed in the roughness-modeled predictions. Examination of the space-time correlation using the elliptic approximation model shows that the roughness-modeled LES underpredicts the convection velocity in the near wall region while overpredicting the sweeping velocity in the outer layer with no improvements observed when refining the grid.

I. INTRODUCTION

Rough-wall-bounded turbulent flows widely exist in nature and engineering applications.[1] Earlier research efforts have been focused on experimental studies of turbulent flows with rough walls (e.g., the works by Colebrook *et al.*[2] and Nikuradse *et al.*[3]). With the exponential growth of the computing power of supercomputers, numerical simulations become popular in the scientific research of rough-wall turbulence. However, roughness-resolved simulations are still not applicable with today's computing power for most real-life, high-Reynolds number, and rough-wall-bounded turbulent flows (e.g., plant canopies[4]). An alternative is to model the effect of rough wall on the outer flow (i.e., roughness-modeled) without directly resolving the flow at the roughness element scale. Studies on rough-wall turbulence have been focused on establishing the relation between the surface drag and the surface topology.[5,6] A few studies were devoted to the development and evaluation of the wall models for rough-wall.[7,8] Toward developing advanced wall models to account for different

geometrical features of rough walls, in this work, we systematically evaluate the predictive capability of roughness-modeled large-eddy simulation (LES) with the logarithmic law wall model using the results from the roughness-resolved direct numerical simulations (DNS).

Different wall models have been developed for rough wall in the literature.[7,8] The logarithmic law for rough wall is one of the classic wall models employed in different applications,[9–11] which can be written in the following form:

$$U^+ = \frac{1}{\kappa} \log \left((y - d)/k_s \right) + 8.5, \qquad (1)$$

where the superscript "+" indicates the scaling in viscous units, i.e., $U^+ = U/u_\tau$ ($u_\tau = \sqrt{\tau_w/\rho}$ is the friction velocity, where ρ is fluid density and τ_w is the total wall stress including the form stress from the roughness elements and the viscous stress), $\kappa \approx 0.4$ is the Kármán constant, k_s is the "equivalent" sand grain roughness, and the zero-plane displacement d is the effective elevation of the boundary layer,

which depends on the rough wall characteristics. In the work by Flores and Jimenez,[12] the rough wall is represented by a smooth wall with nonzero velocity fluctuations in the wall normal direction. Busse and Sandham[4] introduced an extra force term in the Navier–Stokes equations to model the rough wall and examined the effects of different parameters and shape functions for simulating turbulent channel flow. Theoretical models based on the logarithmic law and exponential law were developed in the literature for flows over urban and canopies.[13,14] Suga *et al.*[15] developed an analytical wall function for Reynolds-averaged Navier–Stokes (RANS) simulation of turbulent flows and heat transfer in rib-roughened channel flow. Yang *et al.*[8] proposed a wall model for RANS based on the von Karman–Pohlhausen integral method of shape function with the mean velocity in the roughness sublayer modeled as an exponential analytical function and the wake interaction of rectangular-prism roughness elements considered based on the concept of flow sheltering. Brereton and Yuan[16] modeled the effect of rough surfaces on turbulent boundary-layer as part of a $k - \varepsilon$ closure based on the concept of rough-wall eddy viscosity. Anderson and Meneveau[7] decomposed the surface into resolved and subgrid-scale height contributions with the effects of the unresolved small-scale surface height fluctuations modeled using a local equilibrium wall model.

Evaluations of roughness-modeled LES are rare and limited to mean streamwise velocity profiles and Reynolds stresses. Statistics of turbulence structures, such as the space-time correlations of velocity fluctuations, which are important in many engineering applications, e. g., wind energy[17] and acoustics,[18,19] were not tested. Busse and Sandham[4] evaluated the proposed model by comparing the predicted Reynolds stresses with roughness-resolved DNS. Suga *et al.*[15] compared the mean velocity profiles and Reynolds stresses predicted by RANS with the wall function for rough wall with experimental measurements. Yang *et al.*[8] evaluated the capability of the proposed model in predicting the roughness length and compared the mean velocity profile from the RANS simulations with the logarithmic profile. Brereton and Yuan[16] examined their model in predicting the friction coefficient and mean velocity profile in RANS simulations. In the work by Anderson and Meneveau,[7] the proposed dynamic roughness model for LES was tested using the mean velocity profile and Reynolds stresses. Based on the aforementioned literature review, very a few works have been carried out on the evaluation of rough-wall wall models for LES. Surprisingly, the predictive capability of the roughness-modeled LES with the logarithmic law as the wall model has not been systematically tested yet, especially via roughness-resolved DNS.

High-fidelity data from roughness-resolved simulations are essential for the evaluations of the wall models for rough wall. Roughness-resolved simulations can be carried out using either DNS,[20–22] which directly simulate all turbulence scales, or large-eddy simulation (LES),[23–25] which only simulate the energy-containing large eddies with the subgrid-scale model to account for the effects of unresolved scales. It is computationally expensive to carry out roughness-resolved simulations of turbulent flows over rough walls because the length scale of the roughness element can be orders of magnitudes smaller than the integral scale of the outer flow. Different methods have been employed in the literature to model the geometry of the roughness element. For some cases with regular shape roughness elements, body-fitted grids can be employed. For instance, Ma *et al.*[21,26] employed a body-fitted

method to simulate the rough-wall turbulence over sinusoidal walls. Roughness elements with complex geometries have been modeled using the volume-of-fluid (VOF) method. For instance, Yuan and Jouybari[23] investigated the topographical effects of rough wall on turbulence statistics using the VOF method. Hantsis and Piomelli[27] employed the VOF method to study the effects of roughness on scalar transport. In a recent work, Li *et al.*[25] employed the sharp interface curvilinear immersed boundary method (CURVIB), which can capture the geometry of the roughness element in a more accurate way compared with the diffuse interface method, to simulate the turbulent flow over rough walls and compared their results with those from the VOF method.

In this work, we evaluate the predictive capability of the roughness-modeled LES with the logarithmic law [i.e., Eq. (1)] as the wall model using the roughness-resolved DNS results of turbulent channel flows with rough walls. This study will provide a systematic assessment on the predictive capability of the logarithmic law wall model and indicate possible directions for developing advanced wall models. Specifically, the assessment includes a wide range of turbulence statistics like the mean streamwise velocity, Reynolds stresses, and space-time correlations, in which the last one plays a significant role in many engineering applications (e.g., control of wind turbine wakes[28,29] and turbulence noise[18,19]) but has not been evaluated for wall-modeled LES even for the smooth-wall turbulence. Through this research, the community will learn that modeling roughness using k_s and d is not enough for accurately predicting the space-time correlation, and refining the grid may not improve the predictions for roughness-modeled LES. Improving the predictions of the space-time correlation is one important direction for roughness-modeled LES.

The rest of the paper is organized as follows. We first introduce the employed numerical method and the computational setup in Secs. II and III, respectively. Then, we compare the predictions from the roughness-modeled LES with those from the roughness-resolved DNS in Sec. IV. Finally, we draw the conclusions in Sec. VI.

II. NUMERICAL METHODS

The virtual flow simulator (VFS-Wind) code[30,31] is employed for both roughness-resolved DNS and roughness-modeled simulations. The governing equations are the three-dimensional, unsteady, filtered continuity, and Navier–Stokes equations shown as follows:

$$\frac{\partial u_i}{\partial x_i} = 0, \tag{2}$$

$$\frac{\partial u_i}{\partial t} + \frac{\partial u_i u_j}{\partial x_j} = -\frac{\partial p}{\partial x_i} + \frac{\partial}{\partial x_j}\left(\nu \frac{\partial u_i}{\partial x_j} - \tau_{ij}\right), \tag{3}$$

where x_i ($i = 1, 2,$ and 3) are the Cartesian coordinates, u_i is the ith component of the velocity vector in Cartesian coordinates, ν is the kinematic viscosity, p is the pressure, and τ_{ij} represents the anisotropic part of the subgrid-scale stress tensor, which is modeled by the dynamic subgrid-scale model.[32] The governing equations are discretized in space using a second-order accurate central differencing scheme and integrated in time using the fractional step method.[33] An algebraic multigrid acceleration along with a GMRES solver is used to solve the pressure Poisson equation. A matrix-free Newton–Krylov method is used for solving the discretized momentum equations.

TABLE I. Simulation parameters for the cases carried out in this work. In this table, Re_τ is the Reynolds number based on the friction velocity and the height of channel, n_x, n_y, and n_z are the numbers of grid nodes in the x, y, and z directions, respectively, Δx^+ and Δz^+ are the streamwise and spanwise grid spacings in wall units, respectively, and Δy_1^+ is the distance of the first off-wall grid node from the wall in wall units.

| Case	Rough wall treatment	Re_τ	k_s	$n_x \times n_y \times n_z$	$\Delta x^+ \times \Delta y_1^+ \times \Delta z^+$
RR	Resolved	1077	$0.097h$	$1024 \times 300 \times 512$	$6 \times 0.7 \times 6$
RM1	Modeled	1010	$0.097h$	$64 \times 20 \times 64$	$96 \times 50 \times 48$
RM2	Modeled	1013	$0.097h$	$96 \times 30 \times 96$	$64 \times 33 \times 32$
RM3	Modeled	996	$0.097h$	$128 \times 40 \times 128$	$48 \times 24 \times 24$
RM4	Modeled	1000	$0.018h$	$64 \times 20 \times 64$	$96 \times 50 \times 48$
RM5	Modeled	540	$0.170h$	$64 \times 20 \times 64$	$51 \times 27 \times 51$

In the roughness-resolved DNS, the sharp interface CURVIB method[33] is employed to model the topology of the rough walls, which are generated by randomly rotated ellipsoids as in the literature.[25,34] As the viscous sublayer is resolved in the roughness-resolved DNS, linear interpolation in the wall-normal direction is employed in the CURVIB method to reconstruct the velocity near the rough surface. In the roughness-modeled simulations, a wall-modeled LES based on the logarithmic law for rough wall Eq. (1) is employed. In this approach, the wall shear stress is computed using the tangential velocity at the first off-wall grid point via the logarithmic law Eq. (1) and is provided as the approximate boundary conditions for the outer flow simulations.

III. COMPUTATIONAL SETUP

In this section, we present the computational setup for the simulated cases. As shown in Table I, we carry out five roughness-modeled LES cases, with three of them simulated using different grid resolutions for the same surface roughness length, and the other two for another two different surface roughness lengths, and compare the obtained results with those from the roughness-resolved DNS to examine the predictive capability of the roughness-modeled LES in simulating turbulent channel flows with rough walls. For simplicity, the roughness-resolved DNS and roughness-modeled LES cases will be denoted as "RR" and "RM"

cases, respectively. For the cases with $k_s = 0.097h$, the roughness-resolved DNS is carried out in this work with detailed flow field data saved for systematic evaluations. For the roughness-modeled LES with the other two roughness lengths, the results obtained from the RM4 and RM5 cases are compared with the results from Yuan and Piomelli[34] and Busse et al.,[35] respectively.

In the roughness-resolved DNS, the rough surface as shown in Fig. 1(a) is generated using the virtual sandgrain model proposed by Scotti.[20] In this approach, the bottom surface is partitioned into square tiles of size $2r \times 2r$ with each tile containing a randomly rotated ellipsoid with semiaxes r, $1.4r$, and $2r$ and its center located at $y_0 = -0.5r$ below the lower wall. In the simulated case, the value of r is set as $r/h = 0.07$ corresponding to the fully rough regime, where h is the height of the channel. The size of the computational domain employed in the roughness-resolved DNS is $6h \times h \times 3h$ in the streamwise x, vertical y, and spanwise z directions, respectively. As shown in Table I, the first off-wall grid node is located at $y^+ = 0.7$ from the wall with a total of 73 grid nodes clustered below the roughness crest in the y direction. In the other two directions, the grid spacings in wall units are 6, which are similar to those employed in the literature.[34] In the roughness-modeled LES cases, the size of the computational domain is $6h \times (h-d) \times 3h$ in the x, y, and z directions, respectively, in which the lower wall is shifted up by $d = 0.8r$ for cases RM1, RM2, and RM3, $d = 0.0176h$ for case RM4, and $d = 0$ for case RM5 to satisfy

(a)   (b)
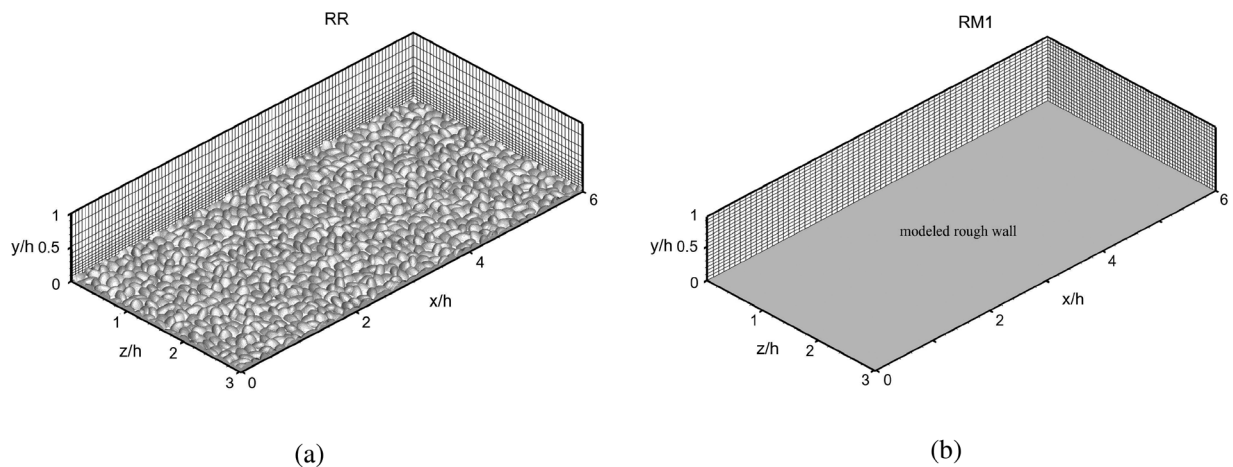
FIG. 1. Schematic for (a) roughness-resolved case and (b) roughness-modeled case. On the slice shown in (a), every 20-grid line is displayed.
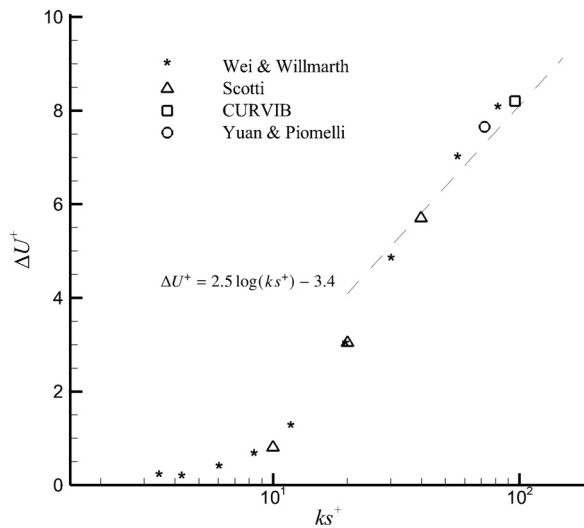
FIG. 2. Comparison of the velocity defect ΔU^+ obtained in this work (CURVIB) and the literature with the analytical relation.

the zero-plane displacement condition. The grid nodes are uniformly distributed in the x, y, and z directions for all RM cases.

The free-slip boundary condition is applied at the top boundary. At the bottom wall, the rough surface is directly simulated using the CURVIB method by applying the no-slip boundary condition at the surface of the roughness elements in the roughness-resolved case. The wall model using the logarithmic law is applied at the bottom wall in the roughness-modeled cases. Periodic boundary conditions are imposed in the streamwise and spanwise directions for all cases. For both RR and RM cases, the flow is driven by a mean pressure gradient to maintain a constant flow rate. The Reynolds numbers $Re_\tau = u_\tau h/\nu$ obtained from the roughness-resolved and roughness-modeled simulations, which is defined based on the channel height h and friction velocity $u_\tau = \sqrt{(\tau_w/\rho)}$ (where τ_w is the wall shear stress), are approximately 1000 as shown in Table I. The flow is first simulated for about

20 flow-through times to achieve a fully developed state. Then, the turbulence statistics are obtained by continuing the simulation for about 45.7 flow through times.

In this work, the "equivalent" sand roughness k_s employed in the RM case is calculated using the RR results by fitting Eq. (1) using the mean velocity profile in the range of $100 < y^+ < 300$. The obtained sand roughness is $k_s = 0.097h$ for RM1, RM2, and RM3 cases, which is higher than the VOF predictions.[20,34] In Fig. 2, the obtained velocity defect from the RR case employed in this work together with others in the literature is compared with the analytical relation between the roughness function ΔU^+ and k_s^+, i.e., $\Delta U^+ = 2.5 \log(k_s^+) - 3.4$, which is derived from Eq. (1) and the following form of the logarithmic law for rough-wall turbulence:

$$U^+(y^+) = \frac{1}{\kappa} \log((y-d)^+) + B - \Delta U^+(k_s^+), \quad (4)$$

where $5 < B < 5.5$ is a universal constant. As seen, the velocity defect and the sand roughness obtained from the RR case simulated using the CURVIB method follow the same trend as others in the literature and collapse well with the analytical relation.

IV. RESULTS

In this section, we compare the results from the roughness-modeled LES with those from the roughness-resolved DNS. It is noticed that in the following comparisons, the origin of y axis is located d below the lower wall of the computational domain for RM cases, which is shifted upward as the zero-plane displacement in the simulations.

We first compare the mean streamwise velocity and Reynolds stresses computed from the RM1, RM2, and RM3 cases with those from the RR case. In Fig. 3(a), we compare the temporally and horizontally averaged streamwise velocity profiles from the RM cases with that from the RR case. It is seen that the mean streamwise velocity profiles from the RM cases agree well with that of the RR case for different grid numbers. In Fig. 3(b), we compare the Reynolds stresses computed from the RM1, RM2, and RM3 cases with that from the RR case. As seen, the overall trends of different terms of the Reynolds stresses computed from the RM cases are similar with that from the
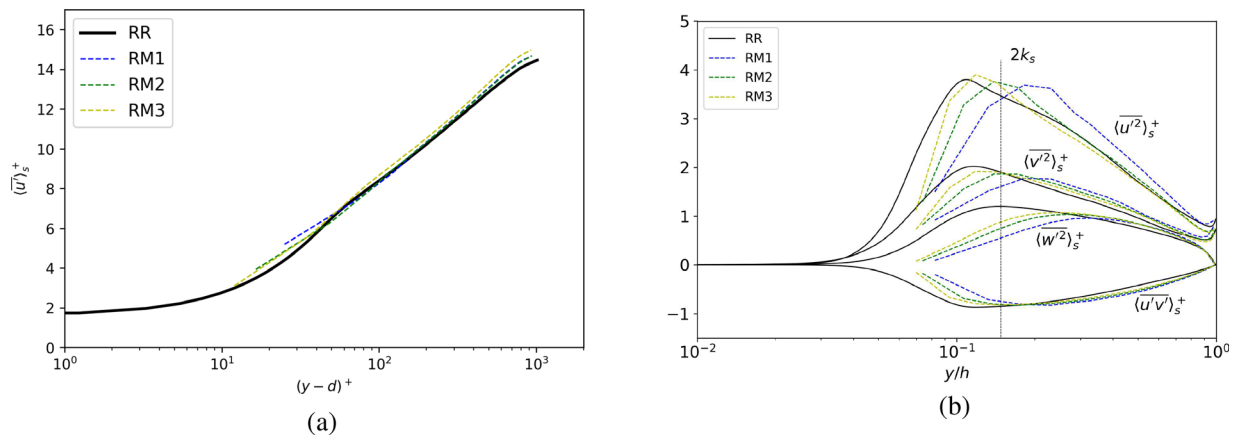

(a)

(b)

FIG. 3. (a) Comparison of the mean streamwise velocity profiles from the RM1, RM2, and RM3 cases with that from the RR case. (b) Comparison of the Reynolds stresses from the RM1, RM2, and RM3 cases with those from the RR case. The Reynolds stresses are normalized using u_τ^2.

RR case. By examining the profiles more carefully, it is seen that in the roughness sublayer (i.e., $y < 2k_s$), the magnitudes of Reynolds stresses from the RM cases are in general lower than those from the RR case. In the outer layer, on the other hand, the Reynolds stresses from the RM cases agree better with the RR case when compared with the comparison in the roughness sublayer. As for the peaks of different components of Reynolds stresses, it is seen that the magnitudes of the peaks computed from the RM cases with different grid resolutions are similar with each other, but with significant different locations for the peaks, which move close to that from the RR case as one refining the grid in the RM cases. The fact that the peaks of the Reynolds stresses predicted by the RR case are located in the roughness sublayer is mainly caused by the disturbed flows induced by the roughness elements. The peaks of the Reynolds stresses predicted by the RM cases, on the other hand, are grid-dependent as for the wall-modeled LES of turbulent channel flows with smooth walls.[36] It is speculated that the peaks from the RM simulations may move even closer to the wall for a grid finer than those employed in the present RM cases.

Comparison for the other two different surface roughness lengths is shown in Fig. 4. Overall, good agreements with measurements are observed for the mean streamwise velocity as shown in Fig. 4(a), although a mismatch less than 4% is observed at $y^+ = 200$ for the RM4 case, for which the roughness length is in the transitional rough regime. The Reynolds stresses computed from the RM4 case are compared with the DNS results from Yuan and Piomelli.[34] It is seen that the magnitudes of the Reynolds stresses computed from the RM4 case agree well with the DNS results in the outer region, while are underpredicted in the near wall region. It is also noticed that the discrepancy of the streamwise component of the Reynolds normal stresses is larger for $k_s = 0.018h$ when compared with that for $k_s = 0.097h$ for the same grid resolution.

We then examine the spatial heterogeneity of the temporally averaged flow field, which is caused by the randomly distributed roughness elements, by analyzing the dispersive stresses,[37,38] which are deduced by decomposing the velocity component u_i as follows:

$$u_i(x, y, z, t) = \langle \overline{u_i} \rangle_s(y) + \tilde{u}_i(x, y, z) + u_i'(x, y, z, t), \quad (5)$$

where $\overline{\cdot}$ denotes temporal averaging and $\langle \cdot \rangle_s$ denotes the superficial average carried out in the whole horizontal plane without considering whether the grid node is located in the fluid or solid.[39] In the above velocity decomposition, $\tilde{u}_i$ describes the spatial heterogeneity caused by the wakes of roughness elements, and u_i' is the turbulent fluctuation. The dispersive stresses are formed by the component $\tilde{u}_i$. In this work, the dispersive stresses $\langle \tilde{u}^2 \rangle$, $\langle \tilde{v}^2 \rangle$, $\langle \tilde{w}^2 \rangle$, and $\langle \tilde{u}\tilde{v} \rangle$ are examined. Different terms of the dispersive stresses are shown in Fig. 5 for different cases. As seen, the streamwise component of the dispersive stresses is comparable with the corresponding component of the Reynolds stress [shown in Fig. 3(b)], while the wall-normal and spanwise components are smaller than those of the Reynolds stresses [shown in Fig. 3(b)]. As mentioned, wakes behind roughness elements are the main cause for the flow heterogeneity for the RR case, which are not resolved in the roughness-modeled simulations. It is clear that these dispersive stresses cannot be predicted in roughness-modeled cases, in which the flow field is uniform in space after the temporal averaging.

After showing the comparisons of the mean streamwise velocity, Reynolds stresses, and dispersive stresses, we examine the capability of roughness-modeled LES in predicting turbulent flow structures. First, we compare the instantaneous velocity fields from the RM cases with those from the RR case in Figs. 6 and 7 on the horizontal planes located at $(y - d)^+ = 100$ ($0.05h$ higher than the crest of the roughness elements located at $y = 1.5r$ in the roughness sublayer) and $(y - d)^+ = 480$, respectively. As shown in Fig. 6, streaks are observed in the contours of the streamwise velocity from both RM1 and RR cases, while those predicted in the RR case have finer flow structures as expected. The reason causing these differences lies on the different flow physics captured by the roughness-modeled and roughness-resolved simulations. In the roughness-resolved cases, the wall-normal velocity fluctuations near the wall are strongly affected by the flow structures at the scale of the roughness element. While in the roughness-modeled simulations, such effects of each individual roughness element are not taken into account. For the spanwise component, some kind of similarity between the RM1 and RR results is observed for the large-scale flow structures, but with more small scale structures resolved in the RR case. For the comparisons at locations further away
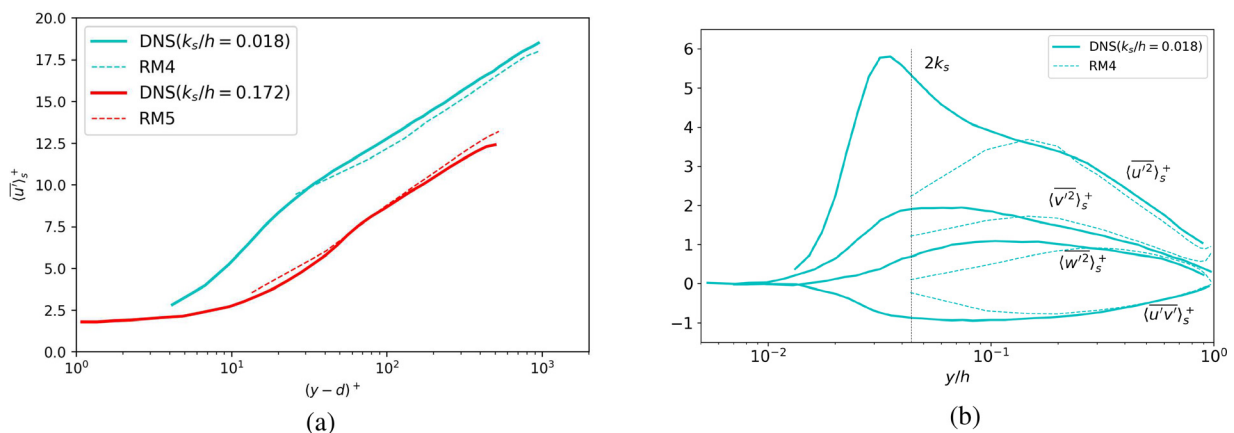

FIG. 4. (a) Comparison of the mean streamwise velocity profiles from wall-modeled LES and DNS of different k_s^+ and Re_τ. (b) Comparison of the Reynolds stresses from the RM4 and those from DNS by Yuan and Piomelli.[34] The Reynolds stresses are normalized using u_τ^2.
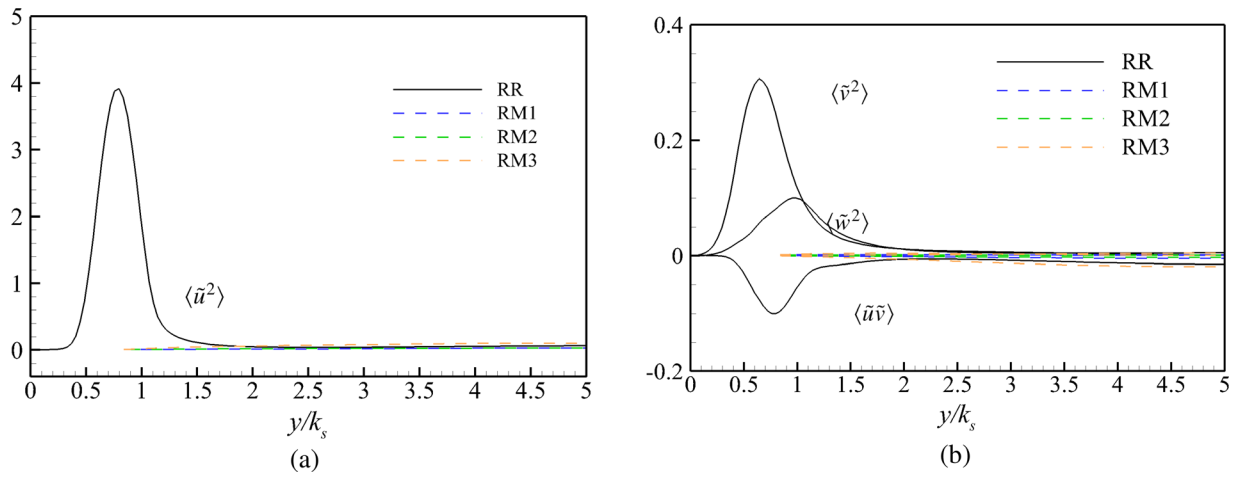
FIG. 5. Comparison of the dispersive stresses from the RM1, RM2, and RM3 cases with those from the RR case for (a) the streamwise component and (b) other components. The dispersive stresses are normalized using u_τ^2.
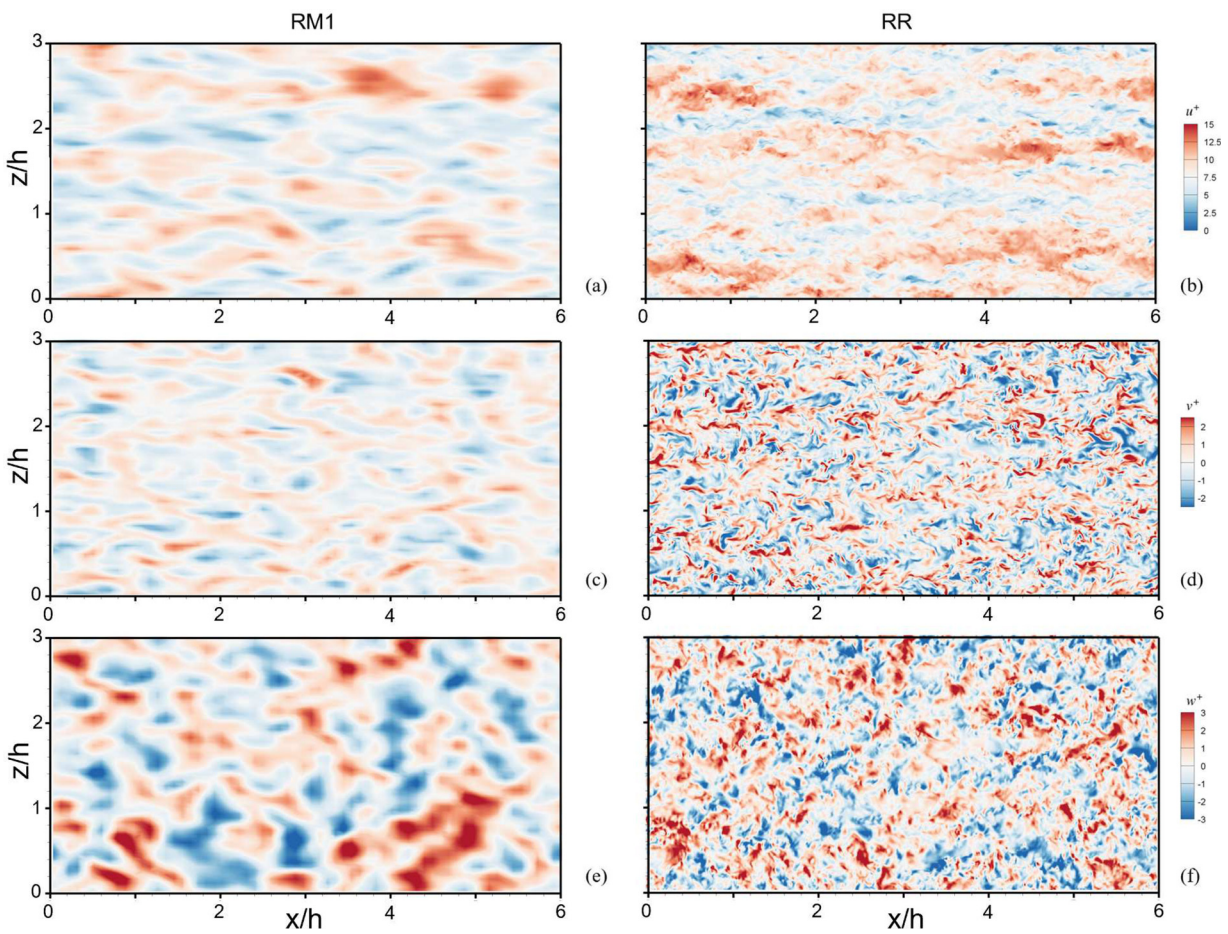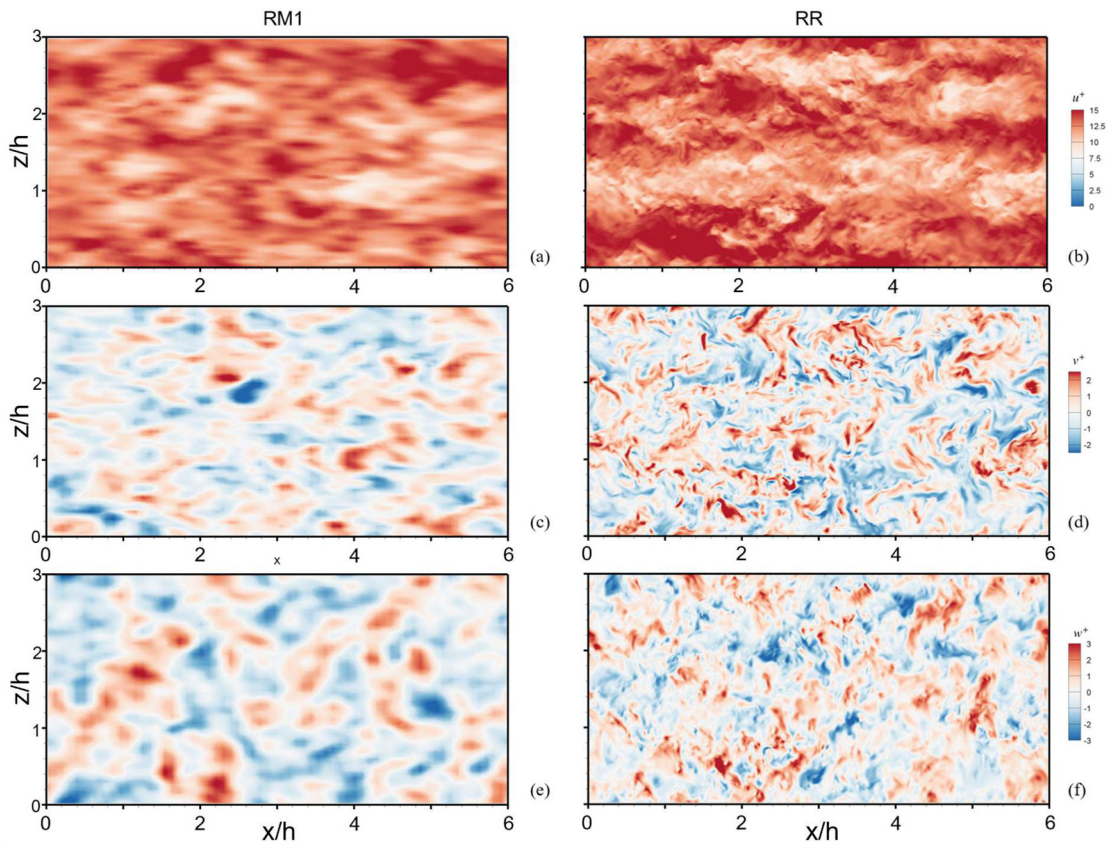

FIG. 6. Comparison between contours of the instantaneous velocity between (a), (c), and (e) the RM1 results and (b), (d), and (f) the RR results for (a) and (b) the streamwise, (c) and (d) the wall-normal, and (e) and (f) the spanwise components, respectively, on the x–y plane at $(y-d)^+ = 100$ from the lower wall.

FIG. 7. Comparison between contours of the instantaneous velocity between (a), (c), and (e) the RM1 results and (b), (d), and (f) the RR results for (a) and (b) the streamwise, (c) and (d) the wall-normal, and (e) and (f) the spanwise components, respectively, on the x–y plane at $(y - d)^+ = 480$ from the lower wall.

from the wall as shown in Fig. 7, the most significant difference between the results from the RM1 and RR cases is that the large-scale streamwise coherent flow structures seen in the roughness-resolved results [Fig. 7(b)] are not well captured by the roughness-modeled LES as shown in Fig. 7(a). For the wall-normal velocity fields, the patterns with large velocity magnitude are roughly aligned with the streamwise component in the RM1 case, which, on the other hand, are of complicated shape in the RR case. For the comparison of the spanwise instantaneous velocity, certain levels of similarity between the RM1 and RR cases are observed for the large-scale flow structures.

To further compare the turbulent flow structures predicted by the roughness-modeled LES with those from the roughness-resolved DNS, we study the two-point space-time correlation of velocity fluctuations, which is defined as follows:

$$R(r, \tau; y) = \frac{\langle u_i'(x + r, y, z, t + \tau) u_i'(x, y, z, t) \rangle}{\langle u_i'^2(x, y, z, t) \rangle}, \quad (6)$$

where r and τ are the space and time separations, respectively. For the present cases, only the streamwise separation is considered with the ensemble averaging performed in time, the streamwise direction, and the spanwise direction at $z/\delta = 0, 0.75, 1.5$, and 2.25. Similar with the comparison of the instantaneous flow fields, the space-time

correlations are examined at two typical wall-normal locations [i.e., $(y - d)^+ = 100, 480$].

We first examine the space correlation $R(r)$ and time correlation $R(\tau)$ separately. The comparisons of the correlations at $(y - d)^+ = 100$ are shown in Fig. 8. For the $R(r)$ and $R(\tau)$ of the streamwise velocity fluctuations shown in Figs. 8(a) and 8(d), it is seen that the correlations predicted by the RM cases on a finer grid agree better with the RR case at small spatial or temporal separations (when R is larger than 0.4). While for larger separations, the correlations predicted by the RM cases decay in a much faster way than the RR case, without improvements when refining the grid. For the wall-normal [Figs. 8(b) and 8(e)] and spanwise [Figs. 8(c) and 8(f)] velocity fluctuations, it is observed that the correlations $R(r)$ and $R(\tau)$ from the RM cases decay to negative before fluctuating around zero as observed in the smooth channel,[40] which, however, is not evident in the roughness-resolved predictions. As refining the grid, the correlations predicted by the RM cases are decreased for small separations, showing a better agreement with the RR case. Figure 9 compares the space correlation $R(r)$ and time correlation $R(\tau)$ from the RM cases with those from the RR case at $(y - d)^+ = 480$. It is seen that for small space or time separations (when $R > 0.6$), the $R(r)$ and $R(\tau)$ of the streamwise velocity predicted by the RM cases (especially the RM3 case) are in good agreement with the predictions from the RR case.
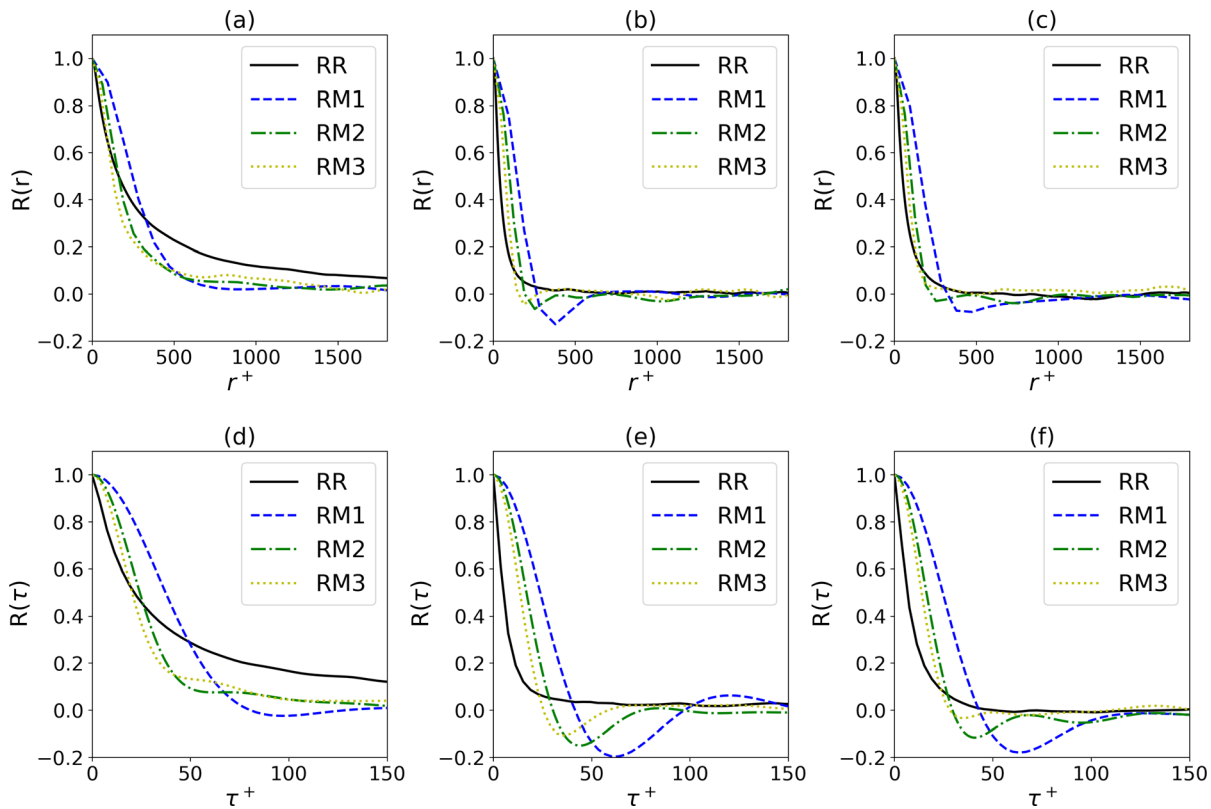
FIG. 8. The streamwise space correlation of (a) streamwise, (b) wall-normal, and (c) spanwise velocity, and time correlation of (d) streamwise, (e) wall-normal, and (f) spanwise velocity averaged in streamwise at $(y-d)^+ = 100$ for different cases.

For large space or time separations, on the other hand, the correlations of the streamwise velocity predicted by the RM cases decay in a much faster way when compared with the RR case. Similar trends were observed at $(y-d)^+ = 100$, while the differences between the RM and RR predictions are larger at $(y-d)^+ = 480$. This is consistent with the observation of the instantaneous streamwise velocity field shown in Fig. 7 that the elongated coherent structures predicted by the roughness-resolved simulations are larger than those from the roughness-modeled simulations at $(y-d)^+ = 480$. For the other two velocity components, the correlations predicted by the RM cases agree better with RR case when compared with those of the streamwise velocity. As refining the grid, improvements are observed for the correlations of the wall-normal and spanwise velocity fluctuations, which are not observed for the streamwise velocity component.

To further examine the capability of roughness-modeled LES in predicting the coherent structures, the length scale λ, which is defined as the separation where the space correlation coefficient of the streamwise velocity decays to 0.5, is examined. Similar method was used by Clark Di Leoni et al.[41] to define a timescale from the time correlation, in order to avoid the error introduced by the fluctuations around zero when defining it as an integral, i.e., $L = \int_0^\infty R(r)dr$. The length scale λ computed from the RM cases is compared with those from the RR case in Fig. 10, in which the λ from the RR case is computed starting from the crest of the roughness elements. It is observed that the length scales computed from the RM cases with different grid resolutions

have similar trends. The values of λ decrease with the increase in the number of grid nodes, with smaller differences observed between the RM2 and RM3 results. The fact that the curves in Fig. 10 all decline near the top of the channel is due to the free-slip boundary condition applied there. Except for such decline caused by the boundary conditions, the length scale, in general, increases as moving away from the wall. When comparing the RM predictions with the RR predictions, it is seen that the length scales computed from the RM cases are larger in the near wall region (when $y^+ < 200 \sim 300$). In the outer region, the length scales from all the RM cases are smaller than those from the RR case, which is consistent with the observations from the instantaneous velocity field shown in Fig. 7.

The iso-contours of the space-time correlations from the RM1, RM2, and RM3 cases are compared with those from the RR case. For the space-time correlations at $(y-d)^+ = 100$ shown in Fig. 11, the iso-contours of correlation coefficients are observed of elliptic shape for high correlation coefficients, although somewhat deviations are observed for the iso-contours of low correlation coefficients.
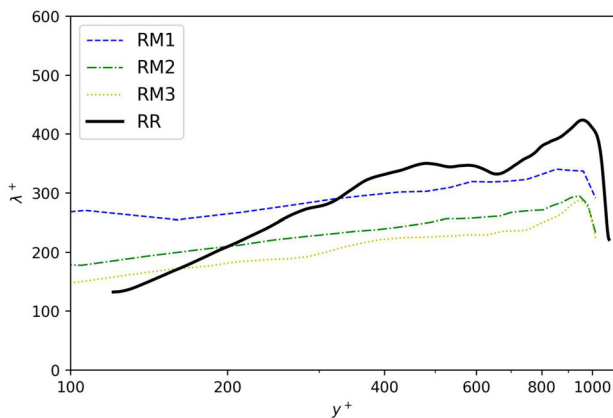
Compared with the RR case, the space-time correlations of the streamwise velocity fluctuations decay slower in the long-axis direction until $R = 0.4$ for the RM1 case.

As one refines the grid, the decay rate increases for $R > 0.4$, which becomes faster for the RM3 case when compared with the RR case. From $R = 0.4$ to 0.2, on the other hand, the correlation coefficient of the streamwise velocity fluctuation computed from the RR case decays
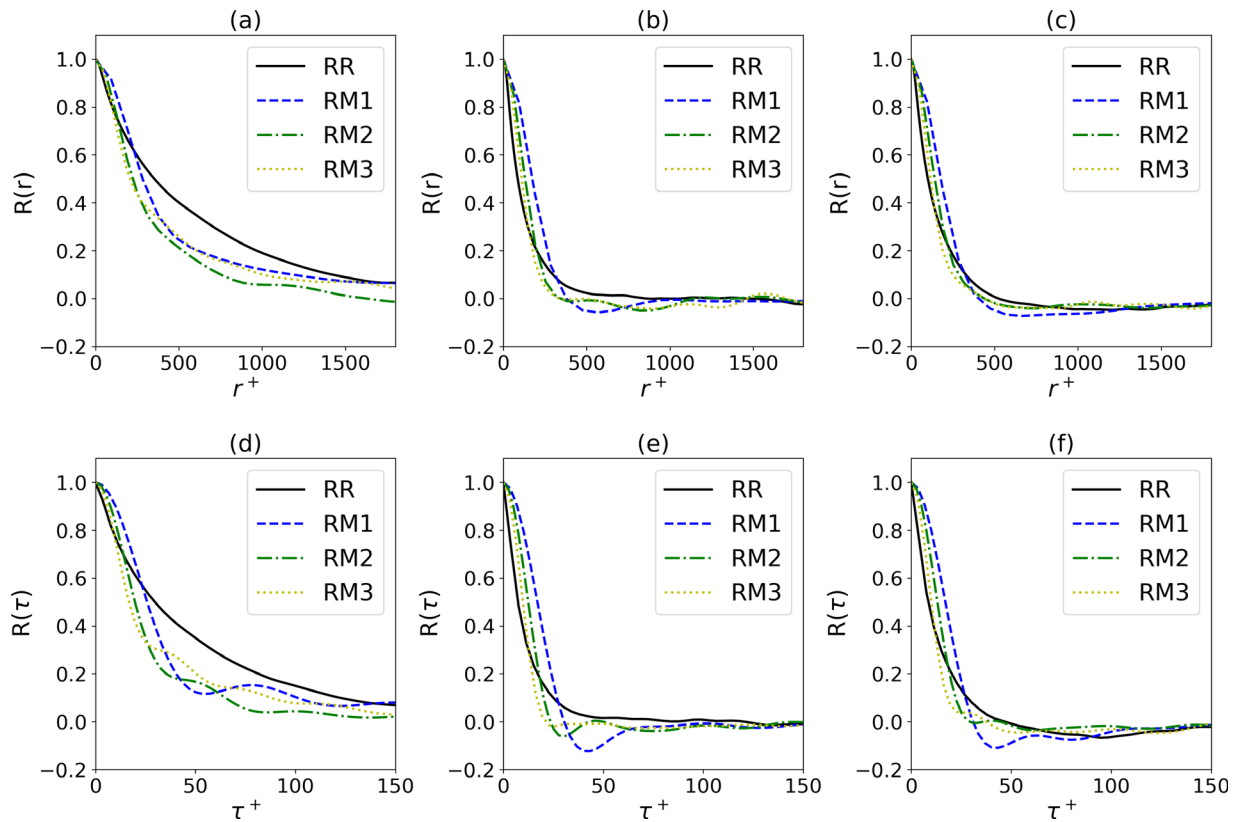
FIG. 9. The streamwise space correlation of (a) streamwise, (b) wall-normal, and (c) spanwise velocity, and time correlation of (d) streamwise, (e) wall-normal, and (f) spanwise velocity averaged in streamwise at $(y - d)^+ = 480$ for different cases.

significantly slower than those from the RM cases. For the space-time correlation coefficients of the other two components of velocity fluctuations, similar differences are observed that the correlation coefficients predicted by the RM cases decay slower than those predicted by the

FIG. 10. Comparison of the length scale λ computed from the RM cases with those from the RR case. The length scale λ is computed as the space separation when the space correlation of the streamwise velocity fluctuations decays to 0.5.

RR case. With the increase in spatial resolutions, agreement with the RR case is improved for the space-time correlations of the wall-normal and spanwise velocity fluctuations. The iso-contours of the space-time correlation at $(y - d)^+ = 480$ are shown in Fig. 12. As seen, the shapes of the isolines are more elongated at this location when compared to those at $(y - d)^+ = 100$. It is observed that the space-time correlations of the streamwise velocity fluctuations from the RM cases decay faster in both long-axis and short-axis directions when compared with the RR results. Refining the grid does not improve predictions. As for the space-time correlations of the wall-normal and spanwise velocity fluctuations, the shape and decay rates computed from the RM cases are similar with those from the RR case.

Based on the elliptic approximation (EA) model proposed by He and Zhang[42] for the space-time correlations in turbulent shear flows, the iso-contours of the streamwise velocity can be modeled as follows:

$$(r - U\tau)^2 + V^2\tau^2 = C, \qquad (7)$$

where U is the convection velocity, V is the sweeping velocity, and C denotes a contour level. Note that the sweeping velocity characterizes the distortion of eddies as they travel downstream, which equals to the sweeping velocity employed in the random sweeping-velocity hypothesis[43] only when the shear rate is zero. In the following, we will examine the geometry features of the ellipse including the length of the major axis a, the length of the minor axis b, and the preferential
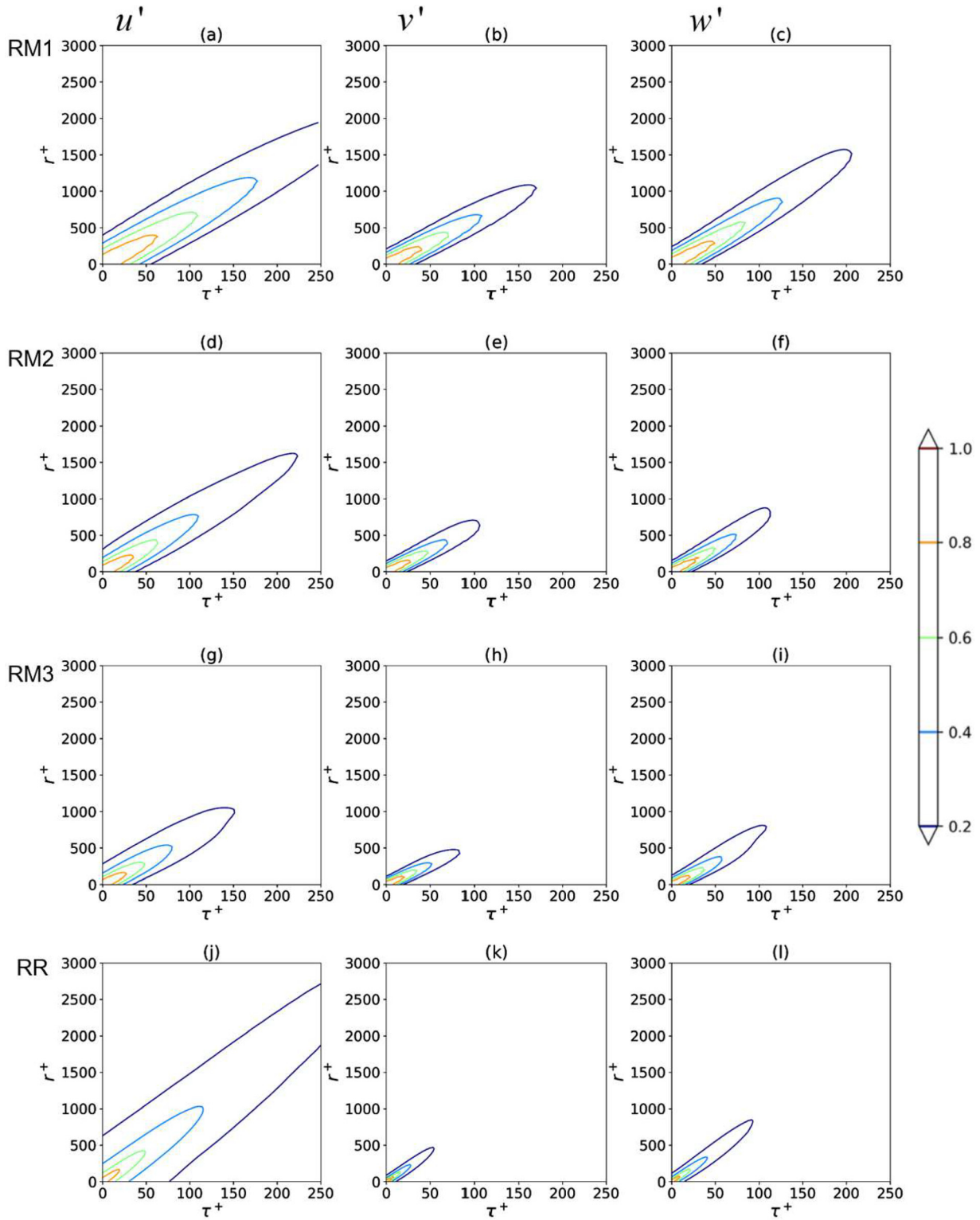
FIG. 11. The iso-contours of the space–time correlations at $(y-d)^+ = 100$ above the lower wall from the RM1 (a)–(c), RM2 (d)–(f), RM3 (g)–(i), and RR (j)–(l) cases, with the first, second, and third columns for the streamwise, wall-normal, and spanwise components, respectively.

FIG. 12. The iso-contours of the space–time correlations at $(y - d)^+ = 480$ above the lower wall from the RM1 (a)–(c), RM2 (d)–(f), RM3 (g)–(i), and RR (j)–(l) cases, with the first, second, and third columns for the streamwise, wall-normal, and spanwise components, respectively.
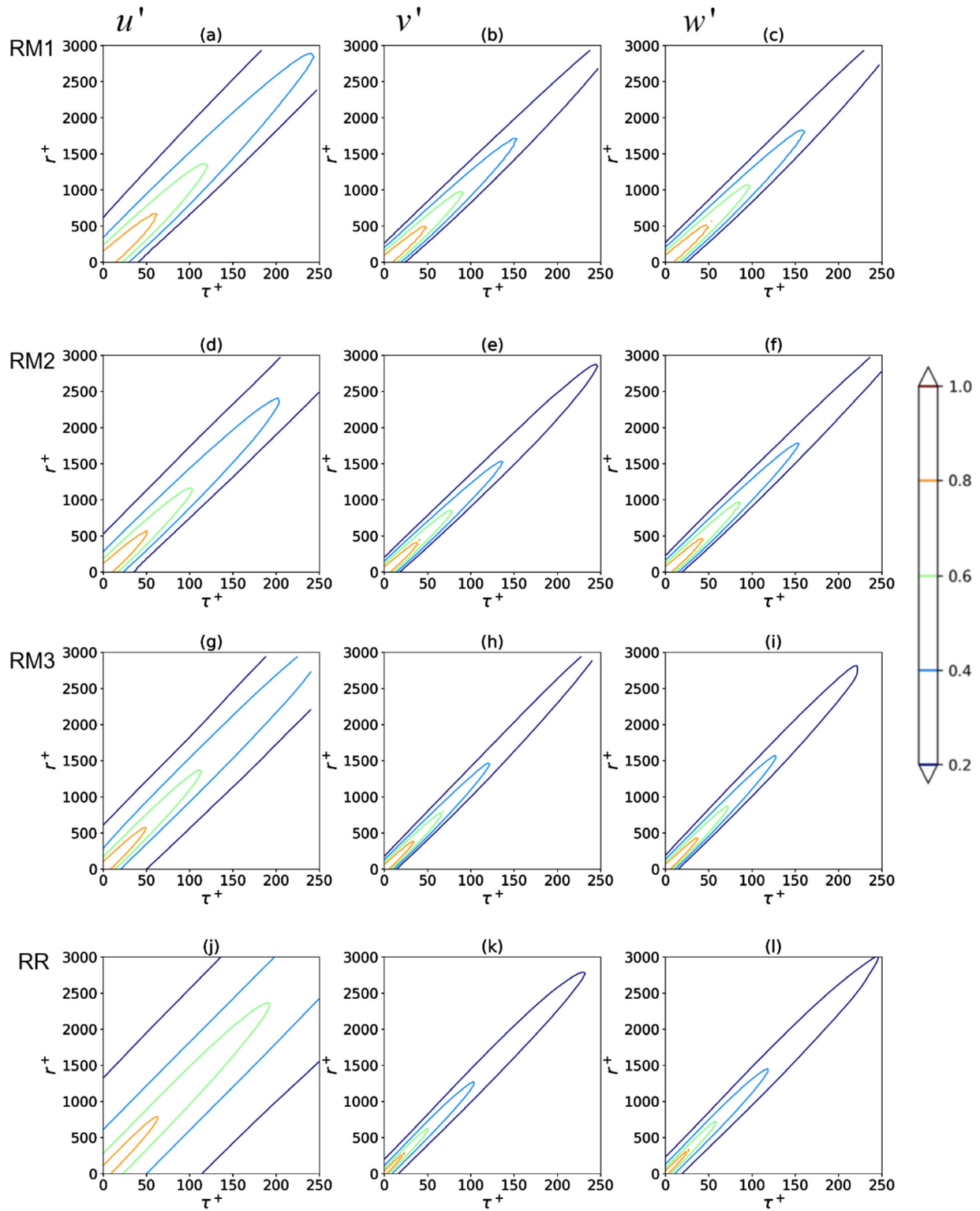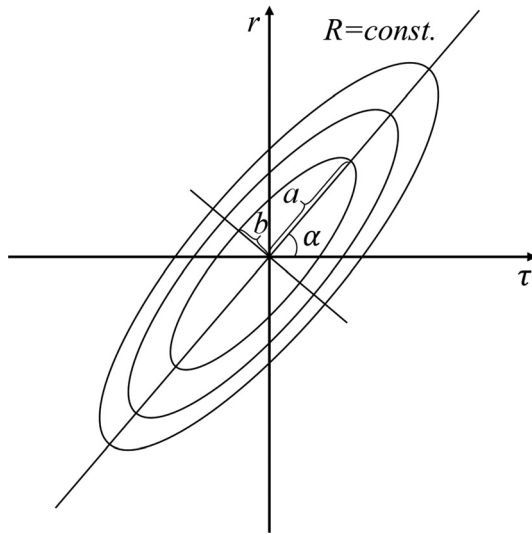
FIG. 13. A schematic for the elliptic approximation model.

direction $\tan(\alpha)$ as demonstrated in Fig. 13. In the present work, the lengths of the major and minor axes are defined as the largest and smallest distances between two points on the ellipse with the connected line passing the origin of the ellipse. With the computed a and b, the aspect ratio $r_a = b/a$ of the ellipse for the iso-contour can then be computed. The preferential direction $\tan(\alpha)$ is defined as the slope of the major axis with respect to the horizontal axis.[44]

In this work, the geometry features including the aspect ratio, the preferential direction, and the lengths of the major and minor axes of the iso-contours of the space-time correlations of the streamwise velocity fluctuations are examined. As seen in Fig. 14(a), the aspect ratios from different RM cases gradually decrease with the increase in temporal separation, being similar with that observed in the RR case. For the range of τ^+ from the RR results, it is observed that the magnitudes of the aspect ratios predicted by the RM cases are larger than those from the RR case. For the preferential directions shown in Fig. 14(b), it is observed that they are approximately the same for different time separations. The preferential directions predicted by the roughness-modeled simulations are smaller than those from the roughness-resolved simulation. As refining the grid, improvement is not observed for RM predictions. For the lengths of the major and minor axes, the predictions from the RM1 simulations are significantly larger than those from the RR simulation, with improvement observed when refining the grid as shown in Figs. 14(c) and 14(d). For the RM3 case, the values of the predicted a^+ and b^+ are closer to those from the RR case for large and small values of $R(r, \tau)$, respectively.

The geometrical features of the iso-contours at $(y - d)^+ = 480$ are shown in Fig. 15. It is observed in Fig. 15(a) that the aspect ratios from the RM cases also decrease with the increase in temporal separation and are closer with that from the RR case as refining the grid. The decrease rates of the aspect ratios computed from the RM cases are similar with each other, but larger than that predicted by the RR case. As for the preferential direction, the predictions from the RM1 and RM2 cases are smaller than those from the RR case with the difference less than 20%. The best agreement with the preferential direction

predicted by the RR case is observed from the RM3 case with the finest grid. However, increasing the grid resolution does not improve the prediction of the decay rate of the space-time correlation, which is high for the RM cases as indicated by the range of the time separations shown in Fig. 15(b). It is also observed the preferential direction, in general, increases when increasing the temporal separation τ^+ for the RM cases, which vary in the opposite way for the RR case. However, it should be noticed that the overall variations of the preferential direction are small for the plotted range of temporal separations. For the lengths of the major axis, the predictions from the RM simulations are smaller than those from the RR simulation, with no significant improvement when refining the grid as shown in Fig. 15(c). The lengths of the minor axes predicted by the RM simulations, on the other hand, are larger than those from the RR simulation for small values of $R(r, \tau)$ for the RM1 case. For the RM3 case, the values of the predicted b^+ are close with those from the RR case for small values of $R(r, \tau)$, while they are smaller for large values of $R(r, \tau)$.

After obtaining the lengths of the major and minor axes and the preferential direction, the convection and sweeping velocity employed in the EA model can be computed via

$$U = \frac{\tan\alpha(1 - r_a^2)}{r_a^2 \tan^2\alpha + 1}, \tag{8}$$

$$V = \frac{r_a(\tan^2\alpha + 1)}{r_a^2 \tan^2\alpha + 1}, \tag{9}$$

which are derived from Eq. (7) and the standard equation of ellipse. The convection and sweeping velocities varying with the temporal separation τ are shown in Fig. 16. It is observed that at both vertical locations [i.e., $(y - d)^+ = 100, 480$], the convection velocities predicted by the RM1 and RM2 simulations are smaller than those predicted by the RR simulation and, in general, increase as the temporal separation increases, which, on the other hand, are approximately the same for different temporal separations for the RR predictions. At $(y - d)^+ = 480$, the convection velocities predicted by the finest grid case, i.e., the RM3 case, are roughly the same with those predicted by the RR case. For the sweeping velocity, the values predicted by the RM cases are, in general, smaller and larger than that from the RR case at $(y - d)^+ = 100$ and 480, respectively, with the prediction from the RM3 case, showing the best agreement with the RR results. The sweeping velocity predicted by the RM cases decreases with the increase in temporal separation at both wall-normal directions, similar with those observed in the RR case.

V. DISCUSSIONS

In this section, we attempt to explain the discrepancies between roughness-modeled LES and DNS from the physics point of view. From the comparisons carried out in this paper, discrepancies were observed in both the near wall region and the outer layer. In the near wall region, the roughness-modeled LES underpredicts the magnitudes of Reynolds stresses, which are predicted reasonable well in the outer layer. In the outer layer, on the other hand, the roughness-modeled LES fails to accurately predict the characteristics of the large-scale flow structures, including the integral length scale and the space-time correlations, for all the considered grid resolutions.

The near wall turbulence is governed by the flows over roughness elements. A large fraction of the drag on the flow is from the form
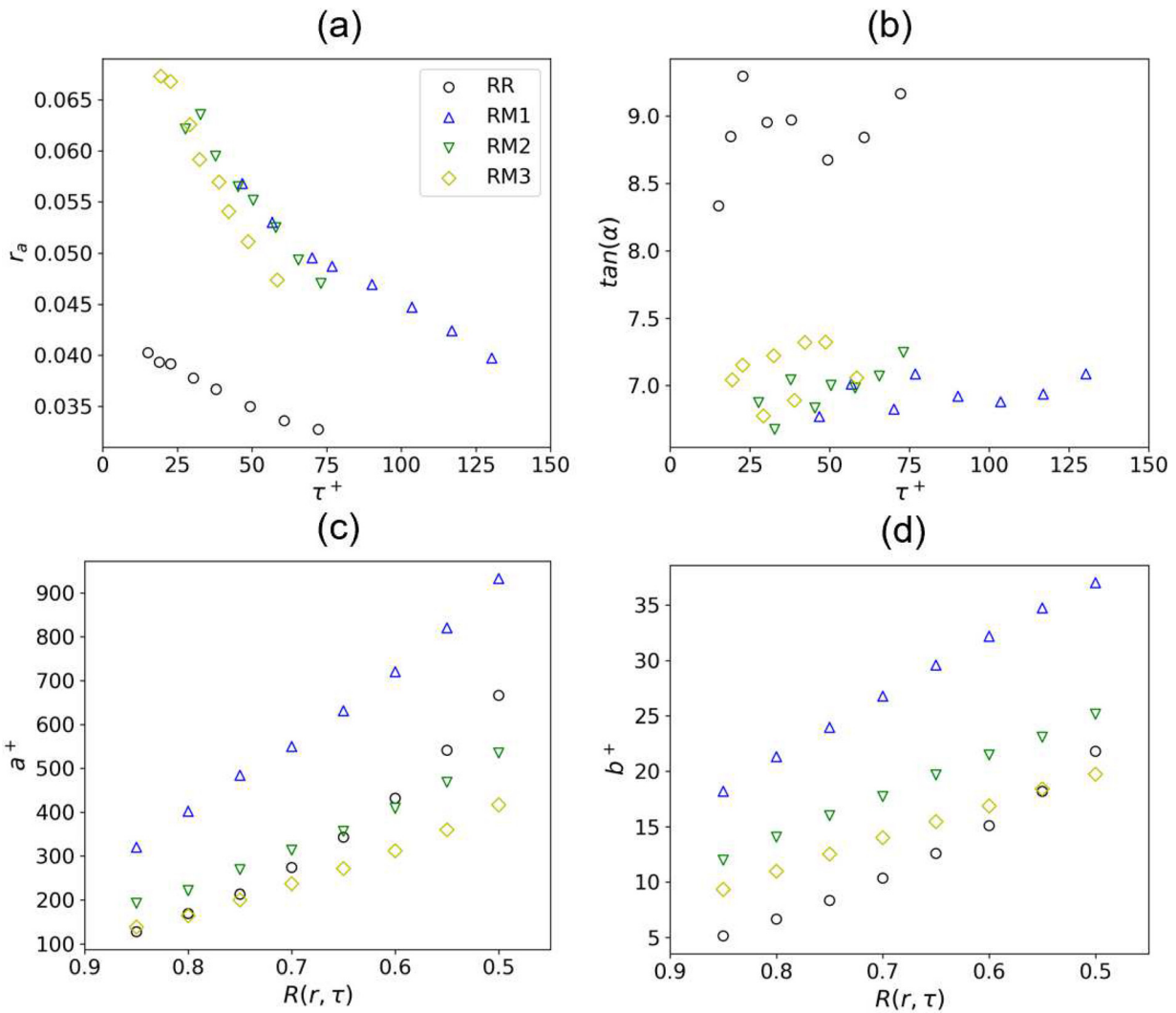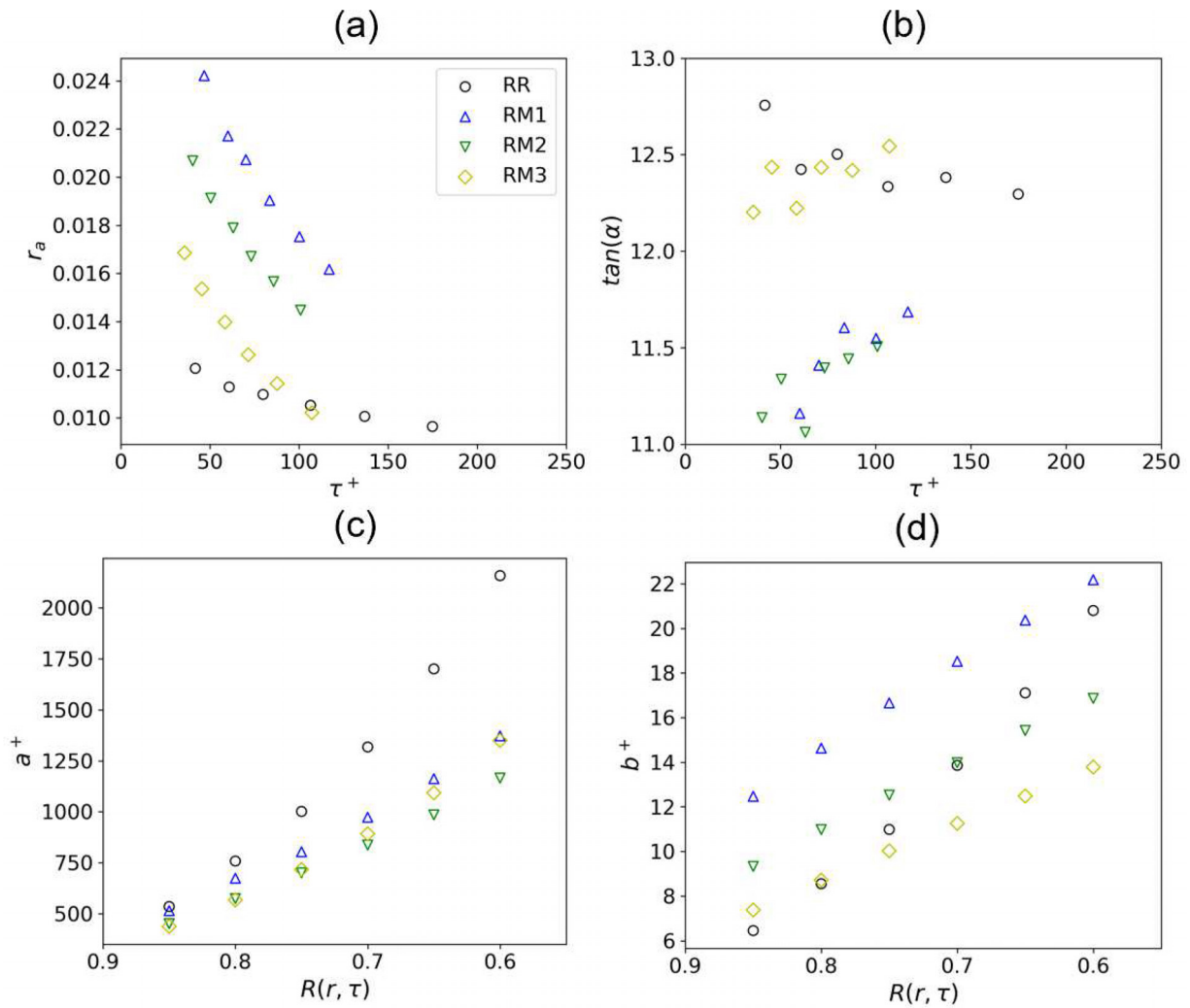
FIG. 14. Geometrical features of the iso-contours of the space–time correlations of the streamwise velocity fluctuations at $(y - d)^+ = 100$ extracted based on elliptic approximation employed in the EA model for (a) the aspect ratios b/a, (b) preferential direction $\tan \alpha$, (c) lengths of the major axes a^+, and (d) lengths of the minor axes b^+ for RR, RM1, RM2, and RM3 cases.

drag on the roughness element. The flow in the roughness sublayer is featured by wakes downstream of the roughness elements. The wake of a roughness element is affected by its shape and orientation, and the wake from the upstream. The wakes, their interactions, and the interaction of wakes with the flow above the roughness sublayer are the key factors affecting the Reynolds stresses (e.g., magnitudes and locations of peaks) in the near wall, indicating that turbulence characteristics in the roughness sublayer will be strongly roughness-dependent. This suggests that it is impossible for the wall model tested in this work to accurately predict the turbulence in the roughness-sublayer, since the mechanisms at the roughness element scale are not properly modeled in the rough-modeled LES.

Similarity exists in the outer layer with the characteristic velocity and length scales set by the flow near the rough wall. Such similarity

was evidenced in the comparisons of the mean streamwise velocity and the Reynolds stresses in the outer layer, where the predictions from the roughness-modeled simulations are similar with those from the roughness-resolved simulations. In the roughness-modeled LES, the velocity scale u_τ is properly modeled by the wall model based on the logarithmic law and employed as wall shear stress boundary condition for the outer flow simulation. The characteristic scale of the rough surface, i.e., the roughness length, although employed in computing wall shear stress, is not explicitly specified in the roughness-modeled LES. Wall similarity holds when the scale of the roughness element is significantly smaller than the boundary layer thickness, e.g., $k/h < 1/40$ proposed by Jimenez[1] and verified by Flack et al.,[45] where k is the height of the roughness element. For roughness elements when k is a fraction of the h, similarity was also observed for the mean flow.[46]

FIG. 15. Geometrical features of the iso-contours of the space–time correlations of the streamwise velocity fluctuations at $(y - d)^+ = 480$ extracted based on elliptic approximation employed in the EA model for (a) the aspect ratios b/a, (b) preferential direction $\tan \alpha$, (c) lengths of the major axes a^+, and (d) lengths of the minor axes b^+ for RR, RM1, RM2, and RM3 cases.

As for the RR case in this work, the equivalent sand roughness is approximately 10% of h and 100 in wall units. Significant interaction between the roughness elements and the outer flow is expected to happen that the roughness elements will affect the turbulence structures in the outer flow as supported by the comparison between the roughness-modeled LES and the roughness-resolved DNS, although similarity in mean flow is still observed. This suggests that wall models for rough wall should properly take into account such interaction between the roughness elements and the outer flow when k/h is not small enough.

VI. CONCLUSIONS

In this work, we evaluated the capability of roughness-modeled LES in predicting turbulent channel flows with rough walls by comparing its predictions with the roughness-resolved DNS results. In the roughness-modeled LES, the rough wall was modeled using the

logarithmic law. In the roughness-resolved DNS, the rough surface, which was generated using ellipsoids with random orientations, was directly resolved using the curvilinear immersed boundary method. Systematic evaluation was carried out for the rough surface with $k_s = 0.097h$, for which three different grid resolutions were considered in the roughness-modeled cases together with the roughness-resolved DNS case. Other two different rough surfaces with $k_s = 0.018h$ and $0.170h$ were also considered for the roughness-modeled cases, with the roughness-modeled predictions compared with the DNS results in the literature.

Turbulence statistics from the roughness-modeled cases were compared with those from the roughness-resolved case. The mean streamwise velocity profiles from the roughness-modeled cases with different grid resolutions agree well with the roughness-resolved predictions. A reasonable agreement between the roughness-modeled and roughness-resolved predictions was observed for the Reynolds stresses
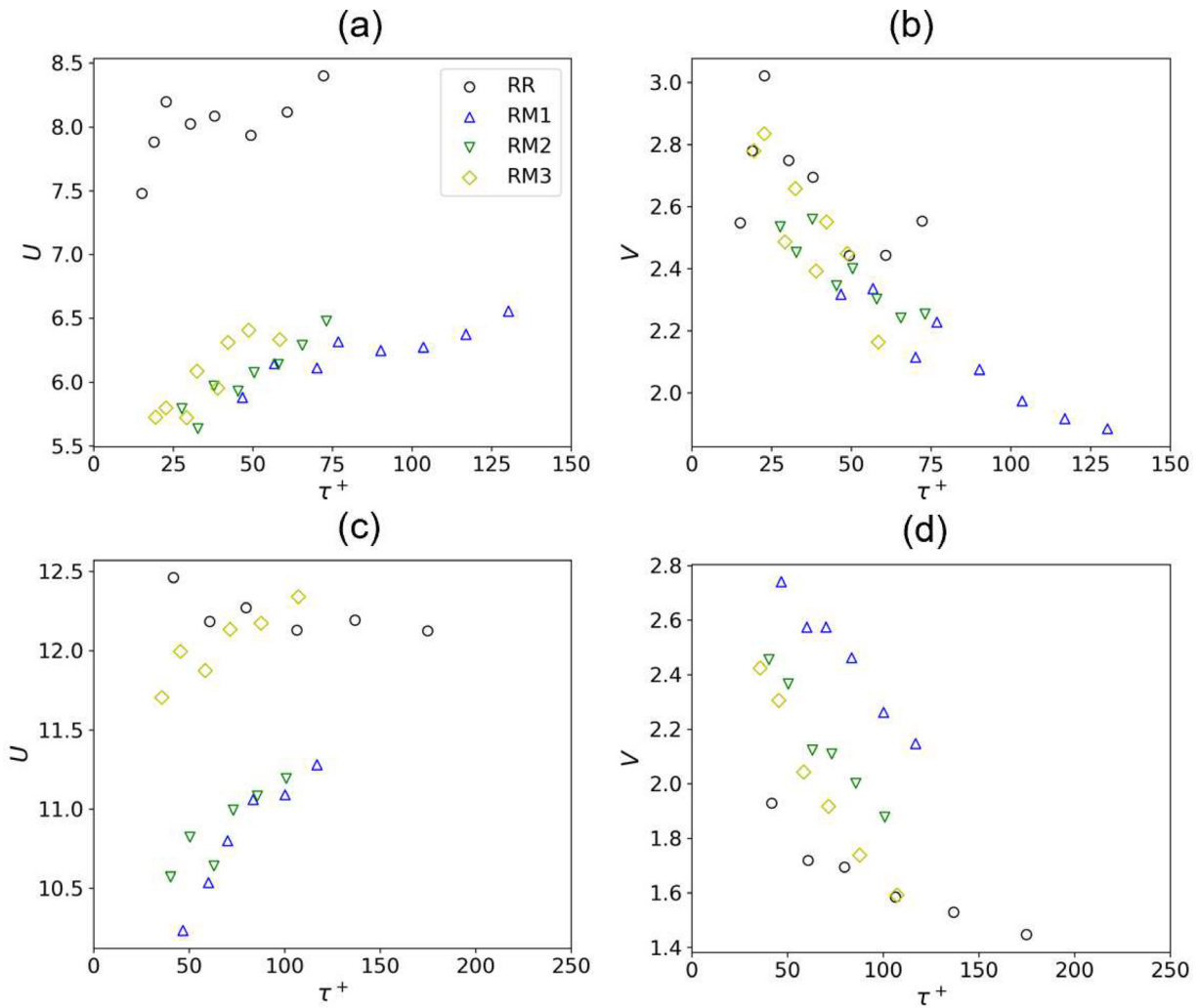
FIG. 16. Convection velocity (a) and (c) and sweeping velocity (b) and (d) computed using Eqs. (8) and (9) with the geometrical features extracted from the iso-contours of the space–time correlations of the streamwise velocity fluctuations (a) and (b) at $(y-d)^+ = 100$ and (c) and (d) at $(y-d)^+ = 480$.

with improvements on finer grids. Significant differences were observed for the dispersive stresses, which cannot be predicted by the roughness-modeled LES. The space-time correlations and the integral scales from the roughness-modeled cases were also compared with the roughness-resolved predictions. It was observed that the integral length scales predicted by the roughness-modeled case reasonably agree with the roughness-resolved predictions in the near wall region for the finest grid, while they are significantly smaller than the roughness-resolved predictions at locations further away from the wall. Large-scale structures in the instantaneous streamwise velocity are not well predicted by the roughness-modeled simulations at locations away from the wall [i.e., $(y-d)^+ = 480$].

For the space-time correlations, the predictions from the roughness-modeled case with the finest grid are acceptable when compared with the roughness-resolved results for the spanwise and vertical velocity fluctuations. However, significant differences were observed for the space-time correlations of the streamwise velocity fluctuations especially at the location further away from the wall [located at $(y-d)^+ = 480$]. No improvements were observed when refining the grid. The iso-contours of the space-time correlations were further analyzed based on the EA model. The convection velocities computed from the roughness-modeled and roughness-resolved cases were compared, with the maximal differences in the range of 10%–20% for $(y-d)^+ = 480$ and about 30% for $(y-d)^+ = 100$, respectively. As for the sweeping velocity, the maximal differences are in the range of 30%–40% at $(y-d)^+ = 480$, which is smaller at $(y-d)^+ = 100$. It was also observed that the variations of the convection velocity with the temporal separations predicted by the RM cases are different from the RR predictions especially at $(y-d)^+ = 480$.

This work has been focused on the evaluation of the logarithmic law wall model, a typical representation of the wall models with the roughness length as the key parameter, using the case the rough surface generated using randomly rotated ellipsoids. Although evaluating different types of wall models for different kinds of rough surfaces is

certainly needed, the findings have general implications: (1) modeling the rough surface using the sandgrain roughness k_s and zero-plane displacement d is probably not enough even for a rough surface with uniform topographic statistics if the objective is to predict the space-time correlation; (2) because of the complex interplay among the grid resolution, the discretization scheme and the subgrid scale model refining the grid do not necessarily result improvements on the predictions for roughness-modeled LES, which is also observed for smooth walls.[36]

The most important takeaway from this work is that representing the rough wall using the roughness length is not enough for accurately predicting the space-time correlations. To predict the space-time correlations, the prediction of the convection velocity for advecting eddies downstream needs to be improved at the near wall locations. At locations away from the wall, on the other hand, one has to improve the prediction of the sweeping velocity, i.e., the distortion of eddies as traveling downstream. The approach for developing the wall models for an improved predictions of the space-time correlations is yet to explore. With the findings of this work, future study will be focused on identifying the key factors affecting the capability of the wall models on predicting the space-time correlations, and developing and evaluating the data-driven wall models,[47] for better taking into account the effects at the roughness element scale and the interaction between the rough wall with the outer flow.

AUTHOR DECLARATIONS
Conflict of Interest

The authors have no conflicts to disclose.

Author Contributions

Shilong Li: Conceptualization (equal); Data curation (lead); Investigation (lead); Methodology (equal); Software (equal); Validation (equal); Visualization (lead); Writing – original draft (lead); Writing – review and editing (equal). **Xiaolei Yang:** Conceptualization (lead); Data curation (equal); Formal analysis (equal); Funding acquisition (lead); Methodology (equal); Project administration (lead); Resources (equal); Software (equal); Supervision (equal); Validation (equal); Visualization (equal); Writing – review and editing (lead). **Yu Lv:** Formal analysis (supporting); Writing – review and editing (supporting).

DATA AVAILABILITY

The data that support the findings of this study are available from the corresponding author upon reasonable request.

REFERENCES

[1]J. Jimenez, "Turbulent flows over rough walls," Annu. Rev. Fluid Mech. **36**, 173–196 (2004).

[2]C. F. Colebrook, T. Blench, H. Chatley, E. Essex, J. Finniecome, G. Lacey, J. Williamson, and G. Macdonald, "Correspondence. Turbulent flow in pipes, with particular reference to the transition region between the smooth and rough pipe laws (includes plates)," J. Inst. Civil Eng. **12**, 393–422 (1939).

[3]J. Nikuradse et al., Laws of Flow in Rough Pipes (National Advisory Committee for Aeronautics Washington, DC, 1950).

[4]A. Busse and N. D. Sandham, "Parametric forcing approach to rough-wall turbulent channel flow," J. Fluid Mech. **712**, 169–202 (2012).

[5]D. Chung, N. Hutchins, M. P. Schultz, and K. A. Flack, "Predicting the drag of rough surfaces," Annu. Rev. Fluid Mech. **53**, 439–471 (2021).

[6]K. A. Flack and M. P. Schultz, "Review of hydraulic roughness scales in the fully rough regime," J. Fluids Eng. **132**, 041203 (2010).

[7]W. Anderson and C. Meneveau, "Dynamic roughness model for large-eddy simulation of turbulent flow over multiscale, fractal-like rough surfaces," J. Fluid Mech. **679**, 288 (2011).

[8]X. I. Yang, J. Sadique, R. Mittal, and C. Meneveau, "Exponential roughness layer and analytical model for turbulent boundary layer flow over rectangular-prism roughness elements," J. Fluid Mech. **789**, 127–165 (2016).

[9]X. Yang, A. Khosronejad, and F. Sotiropoulos, "Large-eddy simulation of a hydrokinetic turbine mounted on an erodible bed," Renewable Energy **113**, 1419–1433 (2017).

[10]A. Khosronejad, T. Le, P. DeWall, N. Bartelt, S. Woldeamlak, X. Yang, and F. Sotiropoulos, "High-fidelity numerical modeling of the Upper Mississippi River under extreme flood condition," Adv. Water Resour. **98**, 97–113 (2016).

[11]Z. Li and X. Yang, "Large-eddy simulation on the similarity between wakes of wind turbines with different yaw angles," J. Fluid Mech. **921**, A11 (2021).

[12]O. Flores and J. Jimenez, "Effect of wall-boundary disturbances on turbulent channel flows," J. Fluid Mech. **566**, 357 (2006).

[13]B.-G. Kim, C. Lee, S. Joo, K.-C. Ryu, S. Kim, D. You, and W.-S. Shim, "Estimation of roughness parameters within sparse urban-like obstacle arrays," Boundary-Layer Meteorol. **139**, 457–485 (2011).

[14]J. Millward-Hopkins, A. Tomlin, L. Ma, D. Ingham, and M. Pourkashanian, "Estimating aerodynamic parameters of urban-like surfaces with heterogeneous building heights," Boundary-Layer Meteorol. **141**, 443–465 (2011).

[15]K. Suga, T. Craft, and H. Iacovides, "An analytical wall-function for turbulent flows and heat transfer over rough walls," Int. J. Heat Fluid Flow **27**, 852–866 (2006).

[16]G. Brereton and J. Yuan, "Wall-roughness eddy viscosity for Reynolds-averaged closures," Int. J. Heat Fluid Flow **73**, 74–81 (2018).

[17]L. J. Lukassen, R. J. A. M. Stevens, C. Meneveau, and M. Wilczek, "Modeling space-time correlations of velocity fluctuations in wind farms," Wind Energy **21**, 474–487 (2018).

[18]M. Wang, J. B. Freund, S. K. Lele et al., "Computational prediction of flow-generated sound," Annu. Rev. Fluid Mech. **38**, 483–512 (2006).

[19]G. He, G. Jin, and Y. Yang, "Space-time correlations and dynamic coupling in turbulent flows," Annu. Rev. Fluid Mech. **49**, 51–70 (2017).

[20]A. Scotti, "Direct numerical simulation of turbulent channel flows with boundary roughened with virtual sandpaper," Phys. Fluids **18**, 031701 (2006).

[21]G.-Z. Ma, C.-X. Xu, H. J. Sung, and W.-X. Huang, "Scaling of rough-wall turbulence by the roughness height and steepness," J. Fluid Mech. **900**, R7 (2020).

[22]M. MacDonald, N. Hutchins, and D. Chung, "Roughness effects in turbulent forced convection," J. Fluid Mech. **861**, 138–162 (2019).

[23]J. Yuan and M. A. Jouybari, "Topographical effects of roughness on turbulence statistics in roughness sublayer," Phys. Rev. Fluids **3**, 114603 (2018).

[24]S. Wu, K. T. Christensen, and C. Pantano, "A study of wall shear stress in turbulent channel flow with hemispherical roughness," J. Fluid Mech. **885**, A16 (2020).

[25]S. Li, X. Yang, G. Jin, and G. He, "Wall-resolved large-eddy simulation of turbulent channel flows with rough walls," Theor. Appl. Mech. Lett. **11**, 100228 (2021).

[26]G.-Z. Ma, C.-X. Xu, H. J. Sung, and W.-X. Huang, "Scaling of rough-wall turbulence in a transitionally rough regime," Phys. Fluids **34**, 031701 (2022).

[27]Z. Hantsis and U. Piomelli, "Roughness effects on scalar transport," Phys. Rev. Fluids **5**, 114607 (2020).

[28]X. Yang and F. Sotiropoulos, "A review on the meandering of wind turbine wakes," Energies **12**, 4725 (2019).

[29]X. Liu, Z. Li, X. Yang, D. Xu, S. Kang, and A. Khosronejad, "Large-eddy simulation of wakes of waked wind turbines," Energies **15**, 2899 (2022).

[30]X. Yang, F. Sotiropoulos, R. J. Conzemius, J. N. Wachtler, and M. B. Strong, "Large-eddy simulation of turbulent flow past wind turbines/farms: The virtual wind simulator (VWiS)," Wind Energy **18**, 2025–2045 (2015).

[31]X. Yang, D. Angelidis, A. Khosronejad, T. Le, S. Kang, A. Gilmanov, L. Ge, I. Borazjani, and A. Calderer, *Virtual Flow Simulator* [Computer Software] (University of Minnesota, 2015).

[32]M. Germano, U. Piomelli, P. Moin, and W. H. Cabot, "A dynamic subgrid-scale eddy viscosity model," Phys. Fluids A: Fluid Dyn. **3**, 1760–1765 (1991).

[33]L. Ge and F. Sotiropoulos, "A numerical method for solving the 3D unsteady incompressible Navier–Stokes equations in curvilinear domains with complex immersed boundaries," J. Comput. Phys. **225**, 1782–1809 (2007).

[34]J. Yuan and U. Piomelli, "Roughness effects on the Reynolds stress budgets in near-wall turbulence," J. Fluid Mech. **760**, R1 (2014).

[35]A. Busse, M. Thakkar, and N. D. Sandham, "Reynolds-number dependence of the near-wall flow over irregular rough surfaces," J. Fluid Mech. **810**, 196–224 (2017).

[36]F. Zhang, Z. Zhou, and X. Yang, "A new single formula for the law of the wall and its application to wall-modeled large-eddy simulation," Eur. J. Mech.—B/Fluids **94**, 350–365 (2022).

[37]V. Nikora, D. Goring, I. McEwan, and G. Griffiths, "Spatially averaged open-channel flow over rough bed," J. Hydraul. Eng. **127**, 123–133 (2001).

[38]E. Mignot, E. Barthélemy, and D. Hurther, "Double-averaging analysis and local flow characterization of near-bed turbulence in gravel-bed channel flows," J. Fluid Mech. **618**, 279–303 (2009).

[39]V. Nikora, I. McEwan, S. McLean, S. Coleman, D. Pokrajac, and R. Walters, "Double-averaging concept for rough-bed open-channel and overland flows: Theoretical background," J. Hydraul. Eng. **133**, 873–883 (2007).

[40]J. Kim, P. Moin, and R. Moser, "Turbulence statistics in fully developed channel flow at low Reynolds number," J. Fluid Mech. **177**, 133–166 (1987).

[41]P. Clark Di Leoni, P. J. Cobelli, P. D. Mininni, P. Dmitruk, and W. Matthaeus, "Quantification of the strength of inertial waves in a rotating turbulent flow," Phys. Fluids **26**, 035106 (2014).

[42]G.-W. He and J.-B. Zhang, "Elliptic model for space-time correlations in turbulent shear flows," Phys. Rev. E **73**, 055303 (2006).

[43]H. Tennekes, "Eulerian and Lagrangian time microscales in isotropic turbulence," J. Fluid Mech. **67**, 561–567 (1975).

[44]X. Zhao and G.-W. He, "Space-time correlations of fluctuating velocities in turbulent shear flows," Phys. Rev. E **79**, 046316 (2009).

[45]K. A. Flack, M. P. Schultz, and T. A. Shapiro, "Experimental support for Townsend's Reynolds number similarity hypothesis on rough walls," Phys. Fluids **17**, 035102 (2005).

[46]K. A. Flack and M. P. Schultz, "Roughness effects on wall-bounded turbulent flows," Phys. Fluids **26**, 101305 (2014).

[47]Z. Zhou, G. He, and X. Yang, "Wall model based on neural networks for LES of turbulent flows over periodic hills," Phys. Rev. Fluids **6**, 054610 (2021).